Three-Dimensional Mapping of Crystalline Ceramic Waste Form Materials

Alex. P. Cocco[1], Matthew B. DeGostin[1], Jacob A. Wrubel[1], Peter J. Damian[1], Tao Hong[2], Yun Xu[2], Yijin Liu[3], Piero Pianetta[3], Jake Amoroso[4], Kyle S. Brinkman[2,*], and Wilson K. S. Chiu[1,*]

[1]*Department of Mechanical Engineering, University of Connecticut, 191 Auditorium Rd., Storrs, Connecticut 06269-3139, USA*

[2]*Department of Materials Science and Engineering, Clemson University, South Carolina 29634, USA*

[3]*Stanford Synchrotron Radiation Lightsource, SLAC National Accelerator Laboratory, 2575 Sand Hill Rd., MS 69 Menlo Park, California 94025, USA*

[4]*Savannah River National Laboratory, Aiken, South Carolina 29808 USA*

[*]*Corresponding authors: ksbrink@clemson.edu; wchiu@engr.uconn.edu*

Abstract:

This work demonstrates the use of synchrotron-based, transmission x-ray microscopy (TXM) and scanning electron microscopy to image the 3-D morphologies and spatial distributions of Ga-doped phases within model, single- and two-phase waste form material systems. Gallium doping levels, which are consistent with those commonly used for nuclear waste immobilization (e.g., $Ba_{1.04}Cs_{0.24}Ga_{2.32}Ti_{5.68}O_{16}$), could be readily imaged. The analysis suggests that a minority phase with different stoichiometry/composition from the primary hollandite phase can be formed by the solid-state ceramic processing route with varying morphology (globular versus cylindrical) as a function of Cs content. The results presented in this work represent a crucial step in developing the tools necessary to gain an improved understanding of the microstructural and chemical properties of waste form materials that influence their durability. This understanding will aid in the future design of higher durability waste form materials.

Background:

Durable ceramic waste forms that incorporate a wide range of radionuclides have the potential to broaden the available disposal options and to lower the storage and disposal costs associated with advanced fuel cycles.[1] These materials, originally developed by Ringwood et al.[2], are often referred to as *SYNROC* (short for "Synthetic Rock"). SYNROC materials comprise ceramic waste forms that are tailored to mimic certain minerals (i.e., unique crystalline structures) that are known to host radionuclides by binding them into specific crystalline networks.[2, 3] The design of ceramic waste form materials is guided by knowledge of naturally occurring minerals, which contain radioactive and non-radioactive species that are elements of concern in waste generated from used nuclear fuel (UNF) reprocessing and weapons production.[4, 5]

In an aqueous reprocessing scenario, four primary waste streams are typically considered: i) a *Cs/Sr* separated stream, ii) a waste stream consisting of *lanthanide fission products*, iii) a *transition metal fission product* waste stream resulting from transuranic extraction, and iv) residual, un-recovered *minor actinides*.[6] Many of the elements in the aqueous reprocessing waste stream are known to react with select additives to form stable SYNROC (titante-based) crystalline phases of the types hollandite[7], perovskite/pyrochlore[8], and zirconolite.[9, 10] These materials are typically densified via hot isostatic pressing (HIP). Recent work, however, has shown that they can also be produced from a melt.[11–13]

A greater understanding of processing conditions on the elemental partitioning, microstructural features, and connectivity of the phases is needed to better design and exploit the properties of ceramic waste forms. Moreover, the impact that 3-D features of a material's microstructure have on its corrosion behavior is needed to assess long-term

waste form performance. For instance, residual porosity that is connected to the material's surface increases the effective surface area available for corrosion. Similarly, in multiphase systems, the preferential corrosion of a particular phase may lead to an increase in porosity and effective surface area. In both cases, the 3-D distribution of phases (including the pores) is central to gaining an improved understanding of the link between microstructure and corrosion behavior in multi-phase waste form materials.

Central to gaining an improved understanding of the connection between 3-D features of a waste form material's microstructure and its corrosion behavior are microstructural imaging techniques. Of particular importance are those techniques that, at a minimum, have the capability to (1) discern multiple material phases and to (2) reveal each phase's spatial distribution, morphology, and connectivity in 3-D.

A number of 3-D imaging techniques exist that meet the basic criteria listed above. Examples include, but are not limited to, magnetic resonance imaging (MRI), transmission electron microscope (TEM) tomography, scanning electron microscopy (SEM)-based stereology, focused ion beam-scanning electron microscope (FIB-SEM) serial sectioning, and x-ray tomography. In recent years, all of these techniques (along with a number of others) have seen increasingly rapid development and widespread application in the study of "energy materials" (i.e., materials used in energy conversion and storage technologies).[14] Similar to *SYNROC*, energy materials design stands to benefit from an improved understanding of how 3-D microstructural features influence material performance.

In choosing a 3-D technique to study ceramic waste form materials, two additional criteria are required. The technique must be (1) capable of imaging dense (i.e.,

high Z) materials and it must (2) offer 3-D resolution on the order of ten's of nanometers with a field of view large enough to capture material volumes on the order of hundreds of cubic microns. Under these conditions, two direct, 3-D imaging techniques – FIB-SEM serial sectioning and synchrotron-based x-ray nanotomography (XNT) – are particularly suitable.

FIB-SEM serial sectioning, a widely accessible and applied technique, produces a 3-D microstructural image by successively imaging and then milling away consecutive, thin slices of material.[14] The sample is destroyed during the imaging process. By exploiting secondary electron contrast using specialized detectors, FIB-SEM is able to discern multiple material phases. The technique's spatial resolution is determined by the 2-D resolution of the SEM (typically single nanometer) and the thickness of each milled slice (often slightly less fine than the SEM resolution, e.g., ~ 5-10 nm). The volume of material that can be imaged using FIB-SEM is relatively large (~1000's of nm^2 field of view) compared to XNT (whose field of view is ~100's of nm^2). Finally, the technique may be performed in conjunction with the SEM's complimentary imaging modes (for example, EDX for chemical mapping in 3-D).

Synchrotron-based XNT makes use of a transmission x-ray microscope (TXM) with a synchrotron x-ray source to perform tomography at 3-D resolutions on the order of 10's of nanometers (e.g., ~20-50 nm).[14] Synchrotron sources are typically housed in government-run facilities that award prospective users "beam-time" through a competitive proposal submission process. As a result, synchrotron-based XNT is less accessible than FIB-SEM. Different material phases are distinguished in XNT by exploiting characteristic x-ray absorption behavior of elements within the phases.

Relative to FIB-SEM, XNT generally offers a smaller field of view (100's of nm^2 as compared to 1000's of nm^2), which means that a smaller volume of material may be considered at a time (although progress is being made in increasing the volume that can be imaged[15]). In contrast to FIB-SEM, XNT is non-destructive, which makes possible the analysis of a single sample by a variety of complimentary techniques, e.g., electron-based imaging or other x-ray methods, such as x-ray fluorescence. Like the SEM, the synchrotron-based TXM, which provides tunable x-ray energy, has a variety of imaging modes that can be used in conjunction with tomography (for example, x-ray absorption near-edge structure XANES spectroscopy to determine chemical bonding states). In contrast to the FIB-SEM's electron beam, hard x-rays exhibit negligible attenuation in a variety of gas atmospheres, which eliminates the need for an evacuated sample chamber. This, along with XNT being non-destructive, makes the technique more readily applicable (as compared to FIB-SEM) for *in situ* imaging.

In this work, synchrotron-based XNT was used to image and characterize ceramic waste form materials in 3-D. The technique's non-destructive image acquisition (which permits the ready application of complimentary characterization techniques) and its potential for *in situ* imaging in future experiments were significant in choosing XNT. (For a more in depth comparison and description of FIB-SEM and XNT as well as a variety of other 3-D imaging techniques, the reader is referred to the reference.[14])

This work demonstrates synchrotron-based XNT as a viable technique for discerning and imaging multiple phases in 3-D in waste form material systems. Moreover, its use in conjunction with complimentary electron- and x-ray-based techniques (i.e., XRD and SEM-EDS) is shown to offer a powerful means of obtaining

insight into 3-D phase morphology and spatial variations in composition. In this case, SEM-EDS and synchrotron-based absorption contrast XNT reveal compositional variations in single-phase, Ga-doped, Cs-containing hollandite.

Introduction: Materials

A Cs-containing hollandite system was chosen for synthesis and 3-D, x-ray-based imaging (in the future work, additional phases and compositions will be considered). Hollandite-type compounds, generally expressed as $A_xM_8O_{16}$, are widely proposed candidates to host and to immobilize Cs in a crystalline waste form.[16–18] Based on current DOE-NE waste streams from potential commercial fuel recycling scenarios, hollandite comprises a large volume fraction of the phase assemblage in multiphase waste forms, and its phase formation is deemed critical to the overall integrity of the waste form material.[6]

Model waste form material systems consisting of (1) Ga-doped, single-phase hollandite and (2) two-phase hollandite + TiO_2 were synthesized using solid-state ceramic processing of oxide powders. In addition to favorable x-ray absorption characteristics, Ga^{+3} is stable in reducing and oxidizing atmospheres and decreases the melting temperature of hollandite.

Three Ga-containing, single-phase hollandite compounds were fabricated for this work: (i) $Ba_{1.33}Ga_{2.66}Ti_{5.34}O_{16}$, (ii) $Ba_{1.04}Cs_{0.24}Ga_{2.32}Ti_{5.68}O_{16}$ and (iii) $Ba_{0.667}Cs_{0.667}Ga_2Ti_6O_{16}$. These compositions are intended to provide insight into the phase formation and microstructural evolution of pure Ba hollandite (sample (i), which contains no Cs), and hollandite with varying amounts of Cs (samples (ii) and (iii)).

Titanium oxide (TiO_2) was selected as the second component for the two-phase waste forms due to its simplicity and prevalence as an additional phase in realistic multi-phase waste forms. The model two-phase, hollandite-TiO_2 material systems were fabricated in both dense and porous forms to evaluate the ability of the imaging technique to discriminate residual porosity. The images collected in this study demonstrate that Ga is an effective dopant for synchrotron-based x-ray imaging methods, in this case, synchrotron-based differential x-ray absorption contrast nanotomography.

Differential X-Ray Absorption Contrast Nanotomography

A transmission x-ray microscope (TXM) is illustrated in Figure 1. Upstream from the microscope, a synchrotron x-ray source and monochromator (not pictured) provide the TXM with a monochromatic beam of x-rays. The monochromatic rays are directed through a pinhole onto the sample by a capillary condenser. In "full-field imaging" (the imaging configuration applied in this work) the entire sample is illuminated (as opposed to imaging by scanning a very small beam across the sample). The sample sits on a rotation stage, which is necessary for tomographic imaging. The x-rays transmitted through the sample are focused onto a CCD x-ray detector by a Fresnel zone plate.

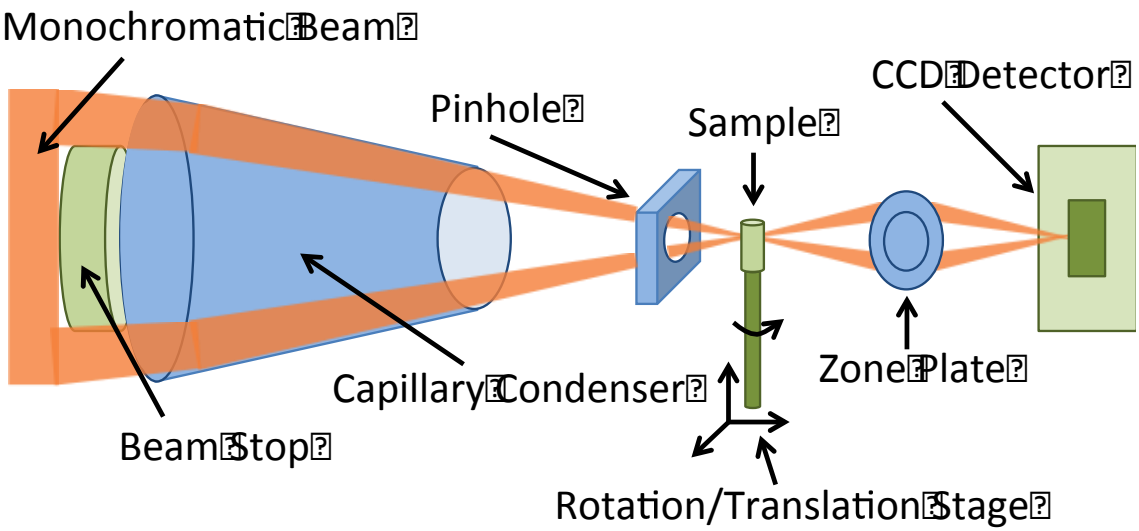

Figure 1: Schematic of a transmission x-ray microscope (TXM).

Contrast in images obtained using a TXM stem from two sources: (1) phase contrast and (2) absorption contrast. Phase contrast, as the name implies, results from changes in incident x-rays' phases as they pass through the sample. Phase contrast typically dominates when imaging low-Z materials using hard x-rays. Absorption contrast, on the other hand, is the result of x-ray attenuation caused by the characteristic x-ray absorption of various elements within the sample. Absorption contrast dominates when imaging dense materials, such as the waste form systems considered in this work.

Fundamental to absorption-based x-ray imaging is Beer's law (Equation 1). Beer's law states that the attenuation of an x-ray beam traveling through a material along a straight line is related to the cumulative effect of the linear attenuation coefficients of the material phases located along that path. In an x-ray absorption imaging experiment, the incident intensity of the x-ray beam $I(0)$ is known and the intensity of the portion of the beam that is transmitted through the material $I(x = L)$ is measured.

$$\ln\left(\frac{I(x=L)}{I(0)}\right) = -\int_0^x k(x^*)\,dx^* \qquad (1)$$

Beer's law indicates that the natural log of the ratio $I(x = L)/I(0)$ summarizes the effective linear attenuation coefficient of the material along the x-ray beam's path: the more strongly attenuating the materials along the path, the lower the intensity of the beam that reaches the detector. Contrast in a two-dimensional image generated by x-rays transmitted through a material (a "projection image"), therefore, reveals linear attenuation coefficient variations and, in turn, variations in material composition (because the linear attenuation coefficient is a material property). In order to determine how the linear attenuation coefficient of the material varies through its cross-section, i.e., in 3-D, tomography is performed.

Tomography refers to the process by which Beer's law, stated for each x-ray beam of a set traversing a slice of material in many directions (a function comprising a set of functions known as a "transform"), is inverted to map spatial variations in the material's linear attenuation coefficient, and thus its phases, over its cross-section.[19, 20] Important to note is that the tomographic process of generating a 3-D image (e.g., the common "filtered back projection" algorithm) assumes that each x-ray beam's deviation from a linear path, e.g., caused by diffraction or refraction, is negligible. As a result, any phenomenon that causes the x-rays to change direction as they travel through the material generates artifacts in the final 3-D image, e.g., streaks across the image or "haloing," whereby a bright artificial edge is created along actual interfaces in the material.

The 3-D spatial distribution of a particular element within a sample (as opposed to a non-specific mapping of relative linear attenuation coefficients) can be mapped using an extension of the tomographic technique called "differential x-ray absorption contrast

tomography" or "absorption contrast tomography" for short.[14, 21, 22] Absorption contrast tomography involves performing tomography twice on a single sample at energy levels above and below the x-ray absorption edges of one (or more) element(s) of interest. An element's x-ray absorption edges correspond to incident x-ray energies, on either side of which the absorption behavior of the element sharply changes.

The calculated "k-absorption edge" (~10.367 keV) for a 15-micron sample of pure Ga, for instance, is shown in Figure 2a. (The transmission data was predicted using the CXRO calculator for X-ray Interactions with Matter (http://henke.lbl.gov/optical_constants).) For incident x-rays at energies below the absorption edge, a 15-micron thick sample of pure Ga transmits close to 75% of the incoming x-ray radiation. Just above the edge, however, the transmission is closer to 10%. The incident photon energy at which this sharp drop in transmission occurs is characteristic to Ga, and more specifically to the interaction of x-rays with electrons in Ga's k shell (x-ray interactions with electrons in Ga's l- and m-shells also have characteristic absorption edges, but the change in absorption behavior is typically less pronounced for shells farther from the nucleus).

The characteristic changes in x-ray absorption behavior that occur for each element in the periodic table act as "fingerprints". For example, if a Ga-containing composite material were imaged just above and just below the characteristic Ga k-absorption edge, any regions in the image that exhibit a change in contrast, i.e., a change from relatively dark to relatively light, must contain Ga (assuming the images taken above and below the edge have each been normalized by the background intensity at each respective energy level and that no other elements' edges overlap with the Ga k-edge).

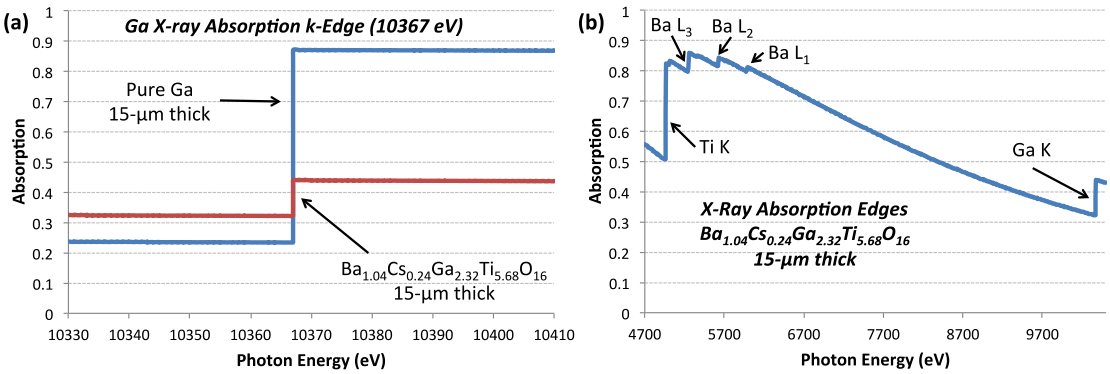

Figure 2: (a) Calcualted x-ray absorption for 15-µm thick samples of pure Ga (blue) and a common Cs-containing hollandite ($Ba_{1.04}Cs_{0.24}Ga_{2.32}Ti_{5.68}O_{16}$) (red). The element's x-ray absorption k-edge is evident at ~10.367 keV. Because the magnitude of the absorption change across the edge depends on Ga content, the change for the hollandite phase is less than that for pure Ga. (b) Calculated x-ray absorption through a 15-µm thick section of hollandite ($Ba_{1.04}Cs_{0.24}Ga_{2.32}Ti_{5.68}O_{16}$). The elemental absorption edges for its component elements are indicated. Ga's k-edge offers the best combination of (1) a relatively large change in absorption and (2) a sufficient photon flux. Calculation of the absorption curves was performed using the CXRO calculator (http://henke.lbl.gov/optical_constants).

That the material contains a given element, however, is not the only information provided by a differential absorption contrast measurement. Because the magnitude of the contrast change across the edge depends on the concentration of the element of interest, the technique also gives a measure of the relative concentration of the element throughout the material. Compare for instance the change in transmission predicted for pure Ga in Figure 2a to that predicted across the same k-edge for a 15 micron thick sample of the Cs-containing, Ga-doped hollandite material ($Ba_{1.04}Cs_{0.24}Ga_{2.32}Ti_{5.68}O_{16}$) shown in Figure 2b. The change in transmission for pure Ga is nearly 65 percentage points whereas the change expected for the hollandite material is closer to 10 percentage points; the higher the concentration of Ga, the greater the contrast change. Thus, differential absorption

contrast XNT makes evident, not only the presence and 3-D spatial distribution of a given element in a material, but also the relative local concentration of that element.

Figure 2b shows edges for each element in the hollandite material ($Ba_{1.04}Cs_{0.24}Ga_{2.32}Ti_{5.68}O_{16}$). In theory, differential absorption contrast imaging could be performed across any of these edges. The Ti k-edge, for example, looks like a promising candidate for imaging given that the magnitude of the absorption change across the edge. In practice, however, imaging at the Ti edge involves reducing the incident x-ray energy to a level that limits the photon flux obtainable for imaging. The limited flux at energies around the Ti k-edge make it necessary to dramatically increase the x-ray exposure time per image and/or to contain the sample in helium in order to minimize any x-ray attenuation in air. Both of these requirements greatly increase the complexity and time required for the imaging experiment. The magnitude of the Ba edges, the other possible alternatives to the Ti and Ga edges, are likely too small to yield significant contrast changes. Thus, the Ga edge was chosen for imaging.

The dependence of the contrast change on elemental concentration has implications regarding sample preparation. First, in order for a given element to be discernable by absorption contrast imaging, its concentration within the sample must be sufficient to yield a measureable contrast change. Thus, for imaging that relies on elemental doping to provide contrast, as in this study of Ga-doped hollandite, the final concentration of the doped element can significantly influence the contrast change measured. Second, the sample's thickness is also influenced by the concentration of the element of interest. Materials with lower concentrations of the element must be thicker. If the concentration is too low, then the volume of material needed to yield sufficient image

contrast can exceed the TXM's field of view, in which case another element may have to be targeted. Finally, it is typically preferable to image a sample that is cylindrical, in which case the path length through the material remains constant as the sample is rotated during tomography. One method for fabricating cylindrical samples for tomographic imaging is by focused ion beam milling.[23]

Experiment

Sample Preparation:

In total three hollandite compositions were considered, each containing a different amount of Cs: (1) a composition without Cs ($Ba_{1.33}Ga_{2.66}Ti_{5.34}O_{16}$); (2) a relatively high Cs content composition ($Ba_{0.667}Cs_{0.667}Ga_2Ti_6O_{16}$); and (3) a composition of intermediate Cs content commonly found in the literature ($Ba_{1.04}Cs_{0.24}Ga_{2.32}Ti_{5.68}O_{16}$).[18]

The hollandite was synthesized by solid-phase reaction. $BaCO_3$, Cs_2CO_3, Ga_2O_3, and TiO_2 (all from Sigma-Aldrich, >99.9%) were mixed in stoichiometry, then ball-milled in ethanol with ZrO_2 milling media for 24 h. The powders were dried and calcined at 1200 ^oC for 10 h to get the hollandite phase. Hollandite pellets were prepared by uniaxially pressing hollandite powders and then sintering them at 1300 ^oC for 2 h in order to densify the resulting composite. (Due to the sinter activity of $Ba_{0.667}Cs_{0.667}Ga_2Ti_6O_{16}$ and $Ba_{1.04}Cs_{0.24}Ga_{2.32}Ti_{5.68}O_{16}$, it was not possible to prepare a completely dense sample.) For the dense, two-phase hollandite-TiO_2 system, 20 *wt*% TiO_2 was added to the hollandite powder, the mixture was ball-milled, and then sintered at 1300 ^oC for 2 h. For the porous, two-phase hollandite-TiO_2 sample, 10 *wt*% graphite was added as a pore former.

Table 1: Density and volume fractions for single-phase hollandite and two-phase hollandite-TiO_2 samples.

Composition	Density	Hollandite/TiO2 Volume Fractions
$Ba_{1.33}Ga_{2.66}Ti_{5.34}O_{16}$	dense	1.0 / 0.0
$Ba_{0.667}Cs_{0.667}Ga_2Ti_6O_{16}$	porous	1.0 / 0.0
$Ba_{1.04}Cs_{0.24}Ga_{2.32}Ti_{5.68}O_{16}$	porous	1.0 / 0.0
$Ba_{1.33}Ga_{2.66}Ti_{5.34}O_{16}/TiO_2$	dense	0.8 / 0.2
$Ba_{1.33}Ga_{2.66}Ti_{5.34}O_{16}/TiO_2$	porous	0.8 / 0.2

Characterization of Phase Composition and Microstructure:

The phase structures of the samples were characterized by x-ray diffraction (Rigaku TTR-III) analysis using Cu K radiation (D/Max-gA) and with 2ϑ from 10 to 70 degree under a speed of 1 degree per minute. The morphology of each hollandite sample was observed using a scanning electron microscope (SEM, Hitachi SU-6600) and their chemical compositions were confirmed using an energy dispersive spectrometer (EDS, Hitachi SU-6600).

Transmission x-ray Microscopy:

Cylindrical samples of the waste form materials for tomographic x-ray imaging were ion-milled using a focused ion beam-scanning electron microscope (FIB-SEM) with a Ga ion beam (Hitachi). The cylinders were approximately 15 μm in diameter and between 15-20 μm in height. They were Pt-welded onto the tips of watch pins, which could then be mounted in the TXM at Beamline 6-2 at the Stanford Synchrotron Radiation Lightsource. The samples were imaged above (10.400 keV) and below (10.334 keV) the Ga k-absorption edge (10.337 keV). The voxel size of the collected images was 40.29 nm. The images were segmented using a watershed algorithm implemented in MATLAB and the segmented volumes were visualized using Avizo.

Results & Discussion

As mentioned above, two types of model waste form systems were examined (1) single-phase hollandite materials with varying Cs content, and (2) two-phase, hollandite/TiO_2 materials, with varying porosity (and no Cs content).

Figure 3 presents the XRD pattern of $Ba_{1.33}Ga_{2.66}Ti_{5.34}O_{16}$ (no Cs), $Ba_{0.667}Cs_{0.667}Ga_2Ti_6O_{16}$ (relatively high Cs content), and $Ba_{1.04}Cs_{0.24}Ga_{2.32}Ti_{5.68}O_{16}$ (intermediate Cs content). The patterns show that $Ba_{1.33}Ga_{2.66}Ti_{5.34}O_{16}$, $Ba_{0.667}Cs_{0.667}Ga_2Ti_6O_{16}$, and $Ba_{1.04}Cs_{0.24}Ga_{2.32}Ti_{5.68}O_{16}$ are all single-phase hollandite. All XRD lines were indexed in the I4/m space group (tetragonal structure) and no parasitic phases were detected. Structural features including lattice parameters were reported in previous work.[18, 24] Due to the larger size of the Cs^+ ion compared to the Ba^{2+} ion, increasing Cs concentration resulted in an increase of the a lattice parameter but with negligible changes to the c lattice parameter.

The XPS spectra of Ba 3d, Cs 3d, Ga 2p, Ti 2p, and O 1s for $Ba_{0.667}Cs_{0.667}Ga_2Ti_6O_{16}$ (higher Cs content) are shown in Figure 4. The Ba, Cs, Ga, Ti and O peaks were fitted at a binding energy, $E_{bind.}$ The fitting results indicated that all elements maintained a fixed valance with no additional peaks observed. For example, Cs 3d displayed one peak at the binding energy 720.5 eV, which is consistent with a previously reported value.[25] No additional peaks were observed to be associated with Cs, which indicated Cs was in a single binding state, a finding consistent with the XRD results that showed no trace of a secondary Cs-containing phase.

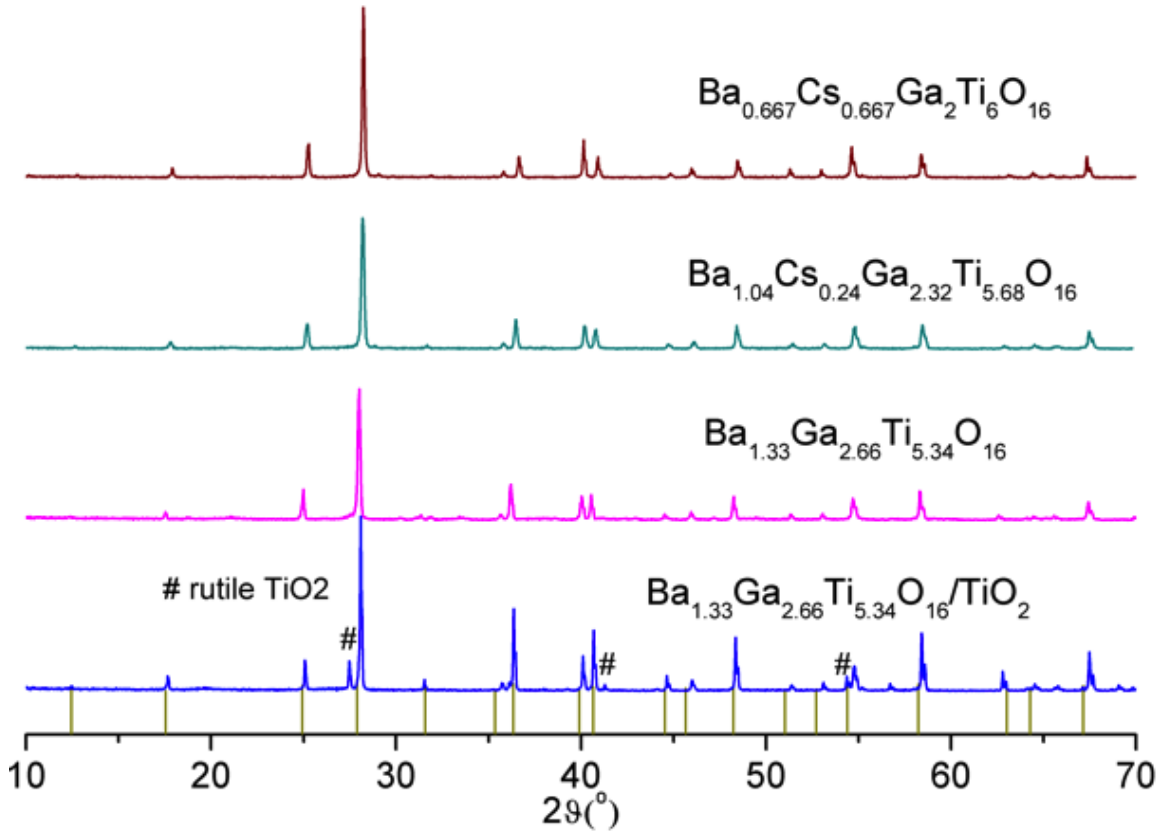

Figure 3: XRD patterns for dense hollandite samples synthesized by sintering at 1300 ^{o}C for 2 h.

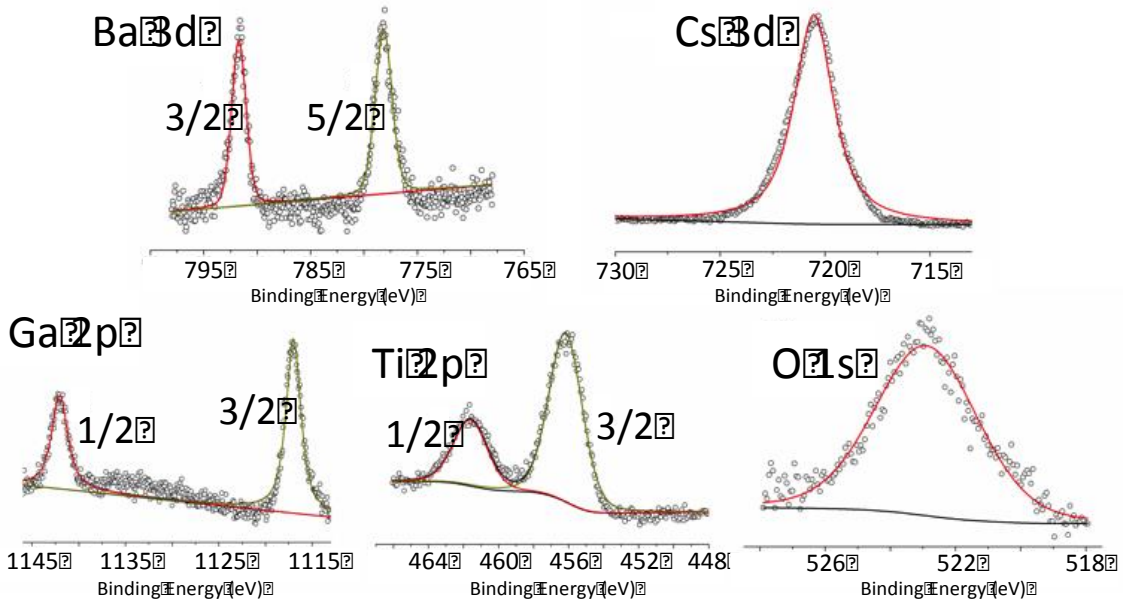

Figure 4. XPS spectra (Ba 3d, Cs 3d, Ga 2p, Ti 2p and O 1s) of the $Ba_{0.667}Cs_{0.667}Ga_2Ti_6O_{16}$ pellet surface; black circles: measured data, black line: the sum of fits, and red/yellow dotted lines: components.

TXM Results for Single-Phase Hollandite Sample without Cs ($Ba_{1.33}Ga_{2.66}Ti_{5.34}O_{16}$)

Synchrotron-based differential x-ray absorption contrast nanotomography was performed on a pure Ba containing hollandite with the composition $Ba_{1.33}Ga_{2.66}Ti_{5.34}O_{16}$. This sample was used to validate the contrast method as a viable tool for investigating the Ga-containing hollandite phase. Because the sample did not contain Cs, and thus could not have any Cs-induced secondary phases, any contrast variation observed across the Ga k-edge would have to correspond to Ga in the Ga-doped hollandite phase as opposed to Ga in a secondary phase containing both Ga and Cs. Furthermore, regions of differing Ga-content would have to come from inhomogeneous doping of the hollandite and, again, not from secondary phases containing both Cs and Ga. Therefore, the sample provided a baseline for determining (1) the uniformity of the Ga doping in the hollandite phase and (2) the contrast change that can be expected for the Ga-doped hollandite phase alone.

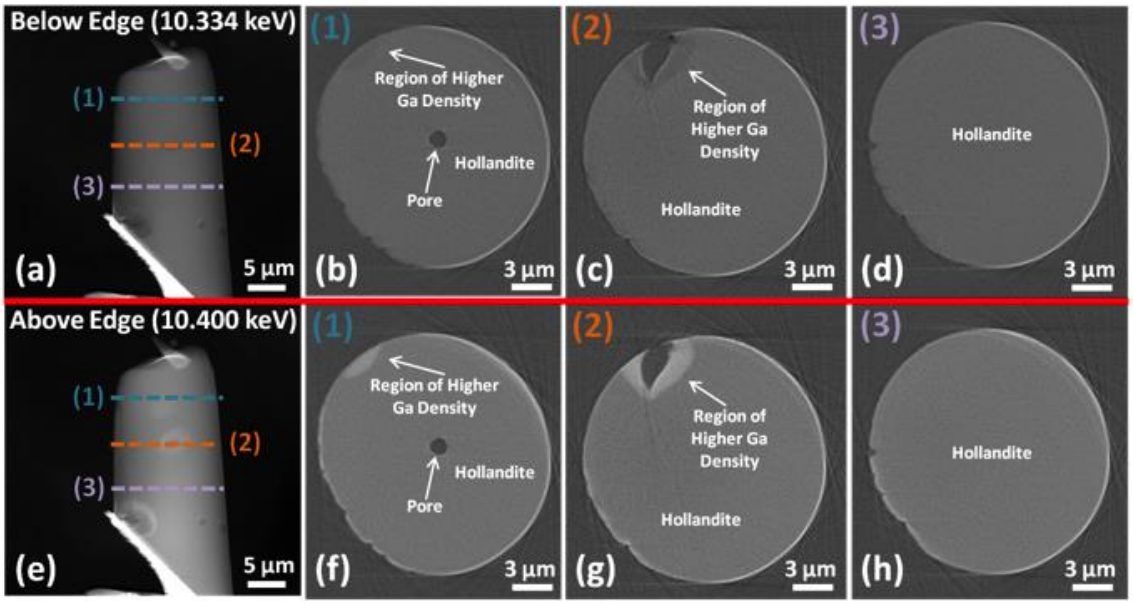

Figure 5: (a) Projection image of a single-phase hollandite waste form sample without Cs ($Ba_{1.33}Ga_{2.66}Ti_{5.34}O_{16}$) obtained below the Ga k-edge. The location of three cross-sections of the material shown in (b-d) are marked on the projection image in (a). Images (e-h) show the same regions of this sample imaged above the Ga k-edge.

Two samples of the baseline material were imaged. Because both yielded virtually identical results with respect to the homogeneity of Ga doping and to the contrast change observed across the Ga k-edge, results for only one sample are presented. Figure 5 shows a projection image as well as representative, reconstructed cross-sections collected at each photon-energy above and below the Ga k-edge. The images reveal that the hollandite's Ga doping is largely homogeneous albeit with some inhomogeneity in Ga content indicated by the regions of starker contrast change across the edge. The regions of higher Ga content accounted for approximately 2% of the sample volume and were found to occur most often around pores (which accounted for approximately 1% of the volume). The Ga-rich regions exhibit a globular morphology, which can be seen in Figure 8a and for an isolated example region in the bottom portion of Figure 8d.

As stated above, because the baseline sample does not contain Cs, the Ga inhomogeneity cannot be attributed to the Cs-induced formation of secondary phases. Another possible explanation would be that the variations in Ga density were introduced during sample preparation, which was done using a Ga FIB. In order to rule out this possibility, the same baseline composition was prepared again using a plasma FIB with a Xe ion beam (FEI Helios P-FIB) and then imaged during a later experiment. The resulting images (shown in the Supplemental Material) also exhibited regions of higher Ga intensity, again close to pores and with globular morphology, thus ruling out Ga implantation during FIB milling as their cause.

A more likely explanation for the Ga-rich regions is that they formed as the result of relatively aggressive Ga doping. In order to obtain maximum contrast change across the Ga absorption edge, high Ga content hollandite stoichiometries were targeted. The baseline composition $Ba_{1.33}Ga_{2.66}Ti_{5.34}O_{16}$ contains close to the maximum Ga concentration expected to be stable in this crystal system, and therefore the baseline may have not fully developed into a homogenously pure phase[26], which resulted in the formation of globular regions of higher Ga content around pores.

The vast majority of the baseline material imaged, however, appears to have been uniformly doped (again Ga-rich regions accounted for only ~2% of the imaged volume) and the pixel intensity for the majority of the hollandite phase changed by roughly 10% across the k-edge. Thus, despite isolated regions of non-uniform Ga-doping, the images of the baseline sample suggest that Ga-doping does in fact provide an effective means of marking hollandite phases for the absorption contrast-based x-ray imaging of waste form materials.

TXM Results for Cs-Containing Samples: ($Ba_{1.04}Cs_{0.24}Ga_{2.32}Ti_{5.68}O_{16}$) & ($Ba_{0.667}Cs_{0.667}Ga_2Ti_6O_{16}$)

Two hollandite samples with differing Cs-content were imaged: (1) a composition typically found in the literature ($Ba_{1.04}Cs_{0.24}Ga_{2.32}Ti_{5.68}O_{16}$), and (2) a composition of higher Cs-content ($Ba_{0.667}Cs_{0.667}Ga_2Ti_6O_{16}$). Like the images of the baseline samples, images of the Cs-containing samples, shown in Figures 7 and 8, reveal a non-uniform distribution of Ga. There is, however, in addition to the globular region that were observed in the baseline sample, another type of Ga variation observed in the Cs-

containing samples: namely, rod-like regions of Ga content higher than the majority of the material volume (~35% contrast change versus a ~10% contrast change across the edge) but less than that of the globular regions (which exhibited a contrast change of ~48% across the edge).

Both types of regions are observed in the intermediate Cs-content sample and can be clearly seen in the 3-D renderings shown in Figure 8b where the Ga-rich, globular regions (~2% of the imaged volume) are shown in green and the rod-like "minority hollandite" (~1% of the volume) in red. (The "majority hollandite" is shown in blue and has been rendered transparent such that the porosity and the green and red phases are viewable.) The porosity accounts for ~11% of the imaged volume.

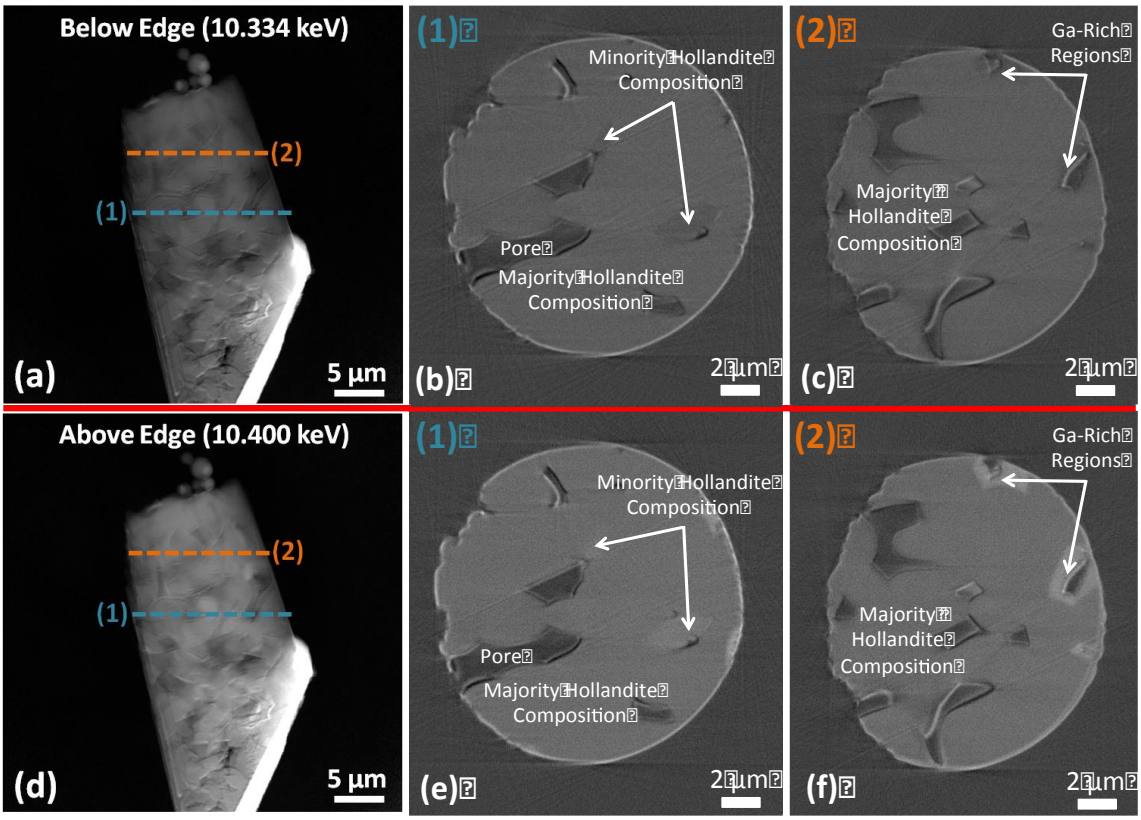

Figure 6: Projection images and reconstructed cross-sections collected above and below the Ga k-edge for a sample with intermediate Cs content ($Ba_{1.04}Cs_{0.24}Ga_{2.32}Ti_{5.68}O_{16}$). Three regions of differing Ga content are observable in the images. As was the case in the

single-phase hollandite without Cs, this sample exhibits globular Ga-rich regions around pores. Then there are two additional Ga-containing phases. The one denoted as the "majority hollandite composition" is very similar to the hollandite phase observed in the baseline sample. The "minority hollandite composition" has higher Ga content than the majority composition, as evident from its starker change in contrast across the edge.

In the higher Cs sample (rendered in Figure 8c), it appears that all Ga-rich regions are rod-like and account for approximately 3% of the sample volume (with porosity being about 12%). The largest complete rod of the minority hollandite in the highest Cs-content sample has been isolated and rendered in the upper portion of Figure 8d in order to clearly illustrate the morphological difference between the minority hollandite and the globular, Ga-rich regions.

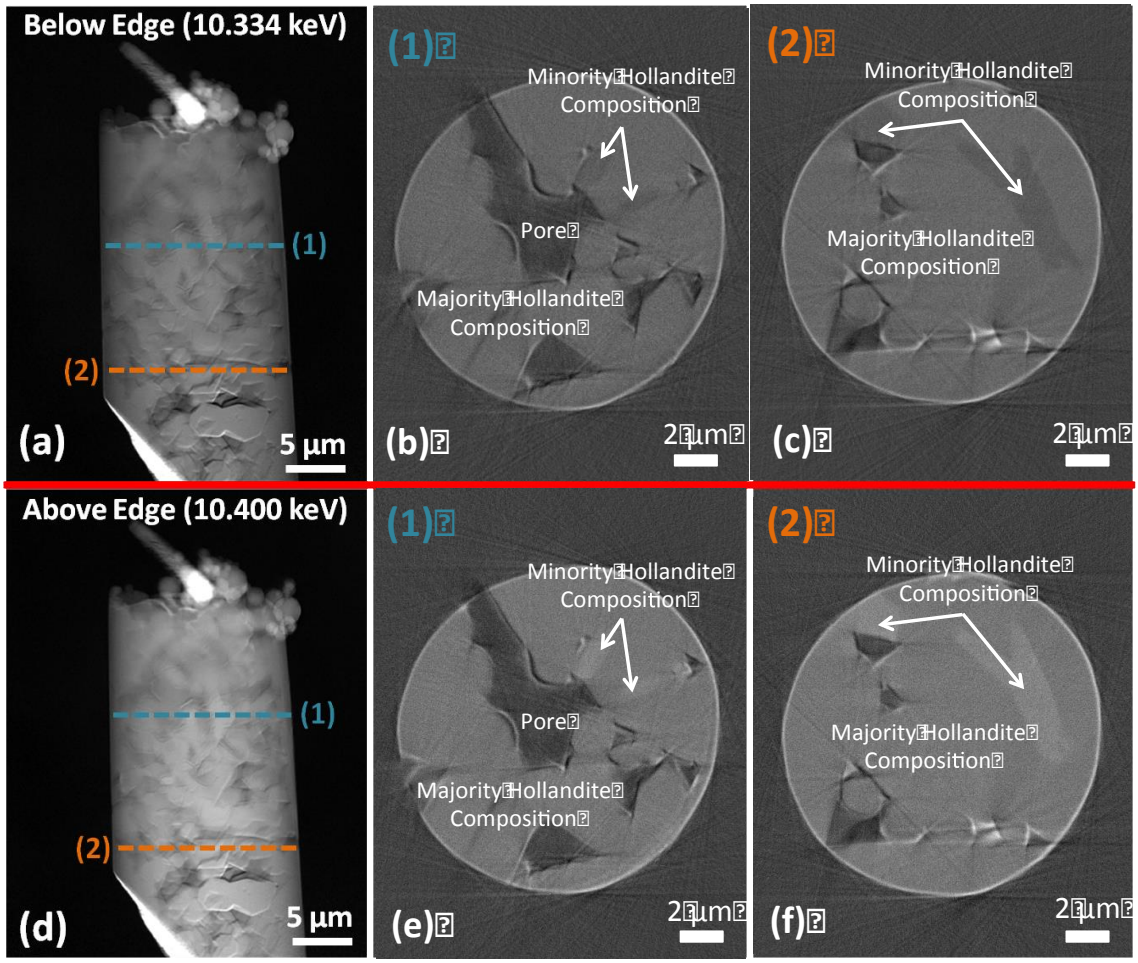

Figure 7: Panels (a) and (d) are projection images collected above and below the Ga k-edge of single-phase, hollandite material with the highest Cs-content of the samples examined ($Ba_{0.667}Cs_{0.667}Ga_2Ti_6O_{16}$). This sample contains the minority and majority hollandite compositions seen in the intermediate Cs-content samples, but does not contain globular, Ga-rich regions near the pores.

Further analysis of these rod-like Ga-rich regions is provided in just after the presentation of the results for the two-phase waste form systems. In the additional analysis, a combination of electron-based microscopy, spectroscopy, and additional analysis of the x-ray images suggest that the "majority" and "minority hollandite" phases are a local variation in the composition of the single-phase hollandite. Before proceeding

to that analysis, however, the remainder of this section presents the x-ray imaging results for the two-phase model waste-form systems, which were intended to demonstrate the ability of the technique to discern two solid phases from pore in waste form material systems.

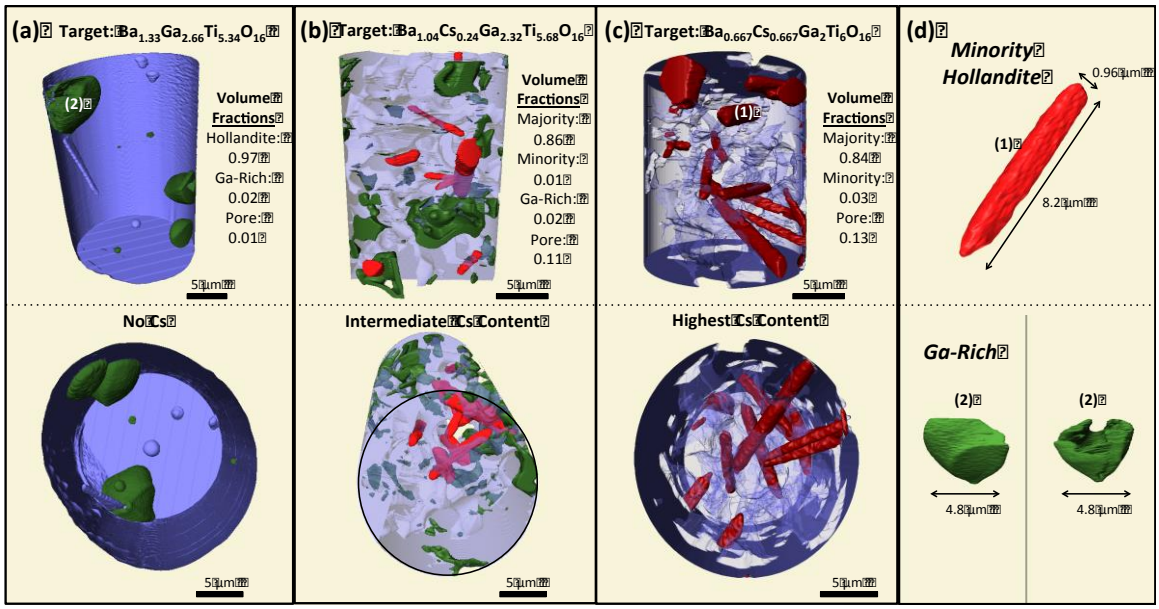

Figure 8: 3-D visualization of the single-phase hollandite (a) without Cs ($Ba_{1.33}Ga_{2.66}Ti_{5.34}O_{16}$), (b) with intermediate Cs content ($Ba_{1.04}Cs_{0.24}Ga_{2.32}Ti_{5.68}O_{16}$), and (c) with high Cs content ($Ba_{0.667}Cs_{0.667}Ga_2Ti_6O_{16}$). Panel (d) shows the two types of differing Ga-content regions found in the samples. The rod-like region in the upper panel was isolated from the higher Cs-content sample and the globular region was taken from the baseline sample without Cs. The intermediate Cs sample is the only one of the three that contains both types of regions.

Two-Phase Model Systems: Dense and Porous Hollandite/TiO_2 Materials

This set of results show images of two-phase, hollandite/TiO_2 waste form systems. Two dual-phase materials were synthesized for study by differential x-ray absorption contrast tomography: (1) a dense and (2) a porous hollandite/TiO_2 material, each with the composition $Ba_{1.33}Ga_{2.66}Ti_{5.34}O_{16}/TiO_2$. In these images, the primary hollandite and TiO_2 phases are discernable from one another, and, in addition, there appear to be multiple

regions of varying Ga content, which are clearly seen in the reconstructed cross-sections. The hollandite in these samples does not contain Cs. Therefore, the Ga-rich regions observed in these samples do not exhibit the rod-like morphology observed in the Cs-containing hollandite examined in the previous section.

Dense Hollandite/TiO_2

Figure 9 shows example projection images and reconstructed cross-sections obtained at each energy level for the dense $Ba_{1.33}Ga_{2.66}Ti_{5.34}O_{16}/TiO_2$ material. The hollandite phase is clearly discernable from the TiO_2. A slight contrast change exhibited by the TiO_2 indicates that Ga incorporated into both phases. Aliovalent Ga doping, Ga^{+3} on Ti^{+4} sites is well known in these materials and low Ga levels in TiO_2 were expected to result from the diffusion of Ga during high temperature sintering.[27]

A small region of higher Ga content was observed in cross-section 1. This region is located at the sample's perimeter and has a globular morphology like the Ga-rich regions seen in the baseline hollandite samples. The very bright region labeled "Platinum" in the second cross-section in Figure 9 is a thin layer of Pt, the material used to secure the samples onto the tips of pins, which were then mounted into the TXM.

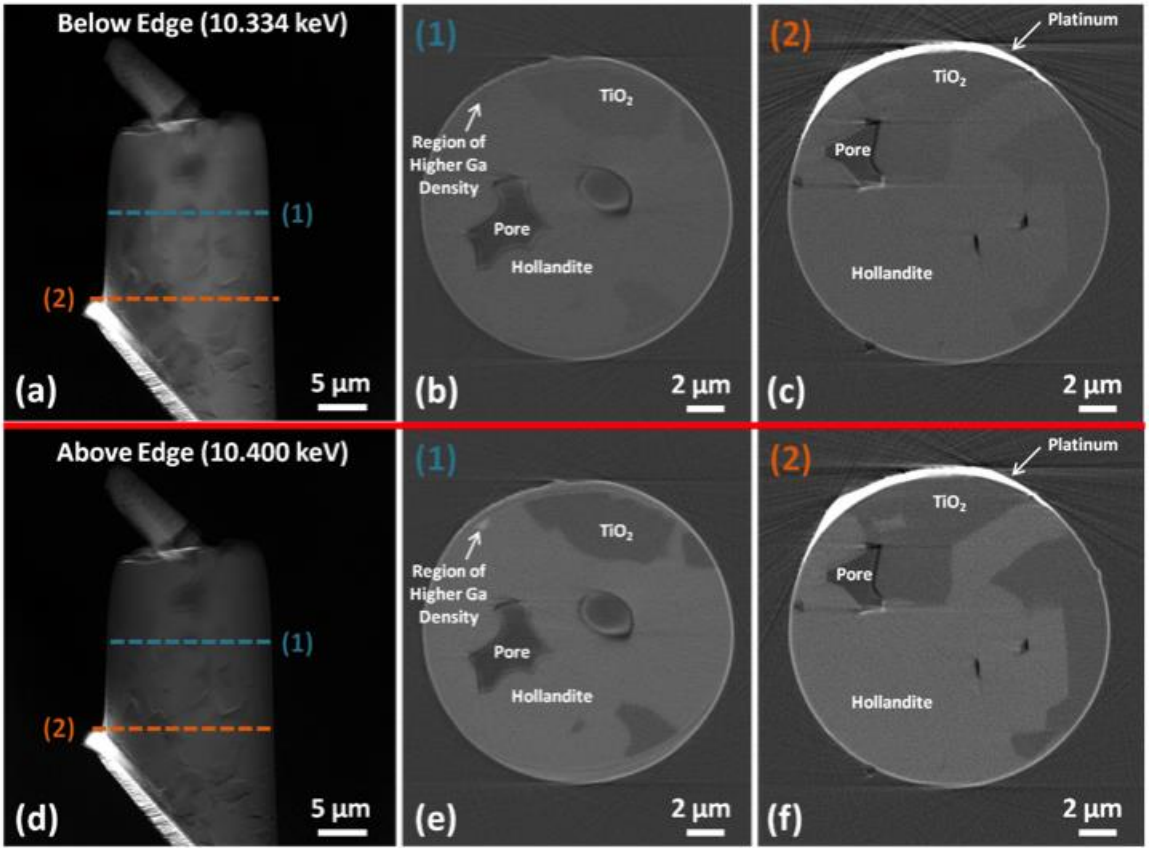

Figure 9: Example projection images and cross-sections obtained from a dense hollandite $Ba_{1.33}Ga_{2.66}Ti_{5.34}O_{16}/TiO_2$ material. The hollandite is clearly discernable from the TiO_2. Because the TiO_2 exhibits a contrast change, it must contain some Ga. A very small region of higher Ga density material is observable in cross-section (1). Pt, which is seen in cross-section 2, was used to weld the samples to the pins that were mounted into the TXM.

Porous Hollandite/TiO_2

Figure 10 present images obtained from 1 of 2 samples that were imaged of the porous, two-phase hollandite $Ba_{1.33}Ga_{2.66}Ti_{5.34}O_{16}/TiO_2$ waste form material. The porous, two-phase system appears to contain many more regions of varying Ga-content than the previous samples. In the baseline hollandite samples, globular Ga-rich regions were observed to occur most often around pores. Increasing the porosity of the system and introducing a second phase (the TiO_2) acts to increase the interfacial area of the

hollandite per volume. This could have potentially made the material more susceptible to Ga inhomogeneity.

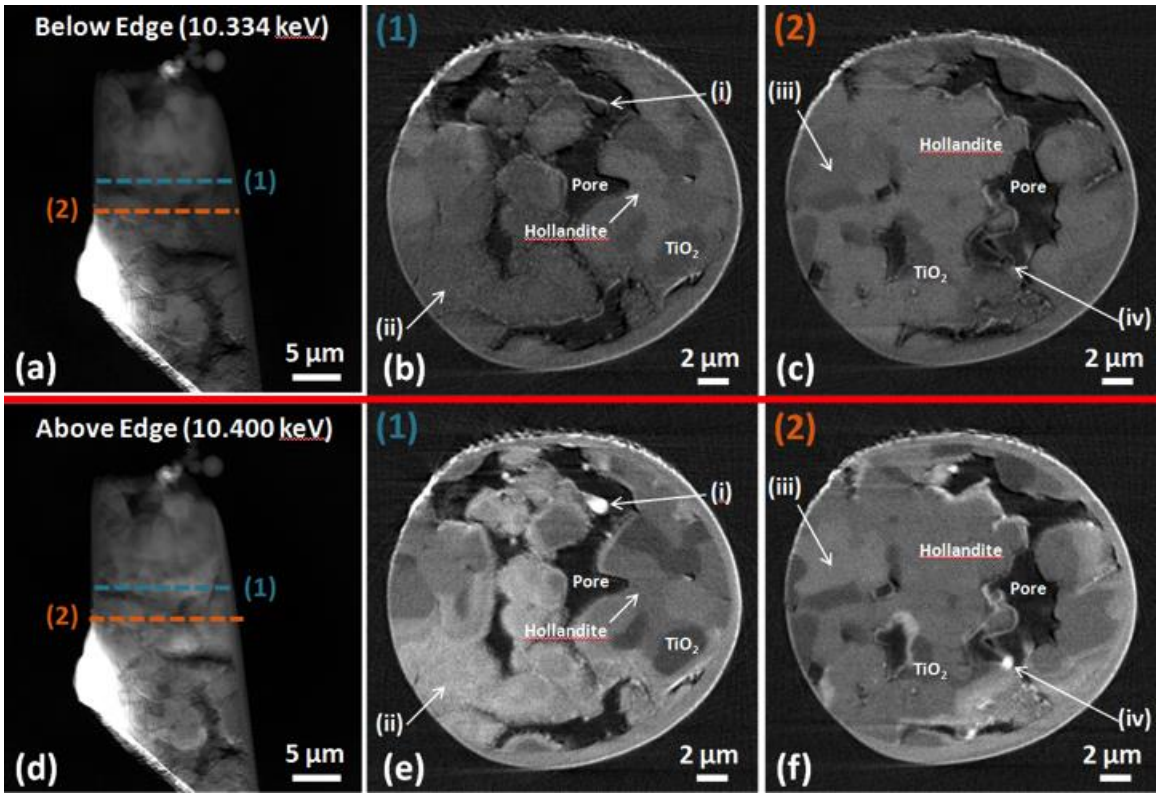

Figure 10: Projection images and cross-sections of a porous hollandite $Ba_{1.33}Ga_{2.66}Ti_{5.34}O_{16}/TiO_2$ sample. At least two additional regions of differing Ga-content to the hollandite, TiO_2, and pore are visible in the reconstructed cross-sections. All of the phases exhibit contrast change when imaged on either side of the Ga k-edge, which indicates that all they contain Ga.

The images of the two-phase model systems demonstrate the ability of the x-ray imaging technique to discern many regions of varying Ga concentration. In order to fully understand the imaging results, however, additional complementary analysis is required. In the following section, further analysis of the rod-like Ga-rich phase observed in the Cs-containing single-phase hollandite samples is peformed that leads to additional insight into the composition of the phase.

Imaging Artifacts

Before moving on, it is important to comment on imaging artifacts present in the TXM images presented above. The artifacts are: (1) a thin higher contrast layer around the perimeter of the sample in the reconstructed cross-sections, and (2) slight "haloing" and "streaking" effects that occurs near the pore/solid interfaces. As was mentioned above, it was confirmed by milling additional samples using a Xe plasma FIB that Ga implantation is not responsible for the Ga-rich regions observed within the samples' volumes. It is, however, likely the source of the high contrast ring around the samples' perimeters. These thin rings exhibit a contrast change across the Ga k-edge and, therefore, must contain Ga. The haloing artifacts that occur around pore-solid interfaces likely result from refraction of the x-ray beams.

The streak artifacts are the result of x-ray diffraction, which resulted as incident x-rays satisfied the Bragg condition for certain grains within the material. Bragg diffraction was clearly observed in the projection images; bright areas in the image suddenly appeared for particular sample orientations and disappeared as soon as the angle of the sample relative to the beam changed. There was negligible change in contrast across the Ga k-edge for the streak regions, indicating that they are indeed artifacts and not caused by local Ga concentration variation. The streaks and haloing artifacts were readily addressed by image segmentation techniques.

Majority & Minority Hollandite Phases

As pointed out in the TXM result, the rod-like Ga-rich phase occupied ~2% and 3% in the intermediate and high Cs-content hollandite samples, respectively. The XRD results presented earlier, however, did not reveal any secondary phases within the detection limit of the technique. This is likely because the detection sensitivity of the XRD technique is approximately 5% volume fraction. SEM-EDS analysis of these samples also did not reveal significant elemental partitioning or segregation to indicate secondary phase formation. Together, these results suggest that the Ga-rich phase observed in the TXM images could be a single hollandite phase with a regions of varying Ga content.

In order to confirm the composition of the Ga-rich phase, SEM-EDS was employed to analyze $Ba_{0.667}Cs_{0.667}Ga_2Ti_6O_{16}$ and $Ba_{1.04}Cs_{0.24}Ga_{2.32}Ti_{5.68}O_{16}$ pellets, as shown in Figure 11. In the mapping result, Ba, Cs, Ti, and O were distributed uniformly on the surface. However Ga exhibited bright spots in the elemental maps. These brighter signals indicate a higher elemental ratio, which is consistent with the TXM result. Estimates of the Ga-rich and common area were obtained by EDS from various points as shown in Figure 12. The EDS point results were recalculated normalizing to Ti (i.e., the Ti stoichiometry was set as the target value). The calculated results are displayed in Table 2.

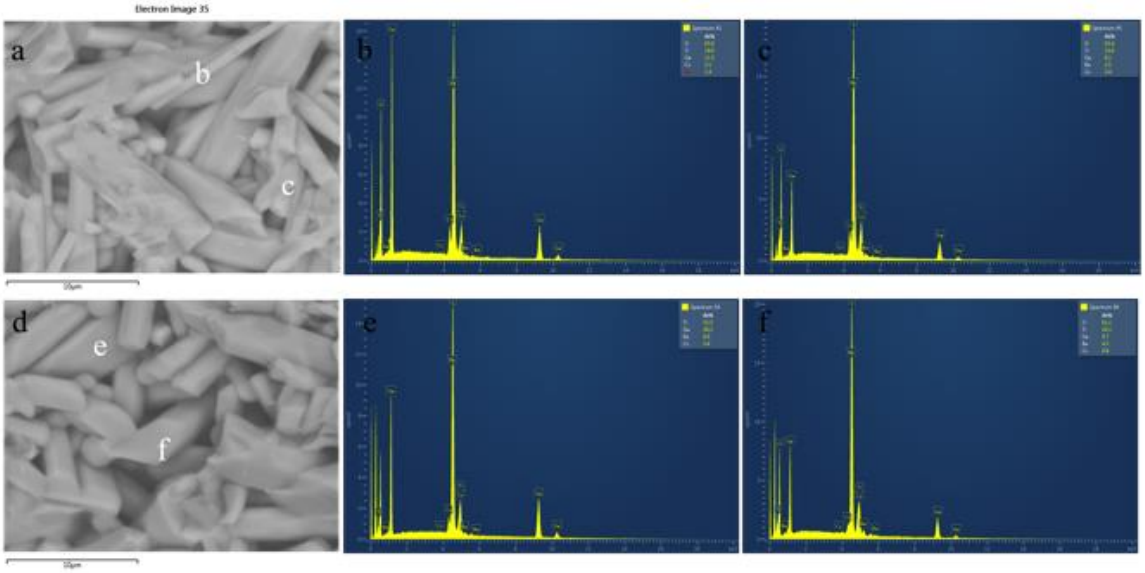

Figure 11: The SEM-EDS mapping images of a) $Ba_{0.667}Cs_{0.667}Ga_2Ti_6O_{16}$ (higher Cs content) and b) $Ba_{1.04}Cs_{0.24}Ga_{2.32}Ti_{5.68}O_{16}$ (intermediate Cs content).

Results for the $Ba_{0.667}Cs_{0.667}Ga_2Ti_6O_{16}$ sample (the higher Cs-content) indicate that the stoichiometry of Ba, Cs, and Ga in the majority phase was 0.633, 0.592 and 1.93 respectively, which is close to the target values 0.667, 0.667 and 2. The $Ba_{1.04}Cs_{0.24}Ga_{2.32}Ti_{5.68}O_{16}$ sample (the intermediate Cs-content commonly found in the literature) displayed similar results for the majority phase. However, in the minority phase, the ratios of Ba, Cs, and Ga varied greatly between samples. The stoichiometry of Ga reached 3.63 and 3.98 in $Ba_{0.667}Cs_{0.667}Ga_2Ti_6O_{16}$ and $Ba_{1.04}Cs_{0.24}Ga_{2.32}Ti_{5.68}O_{16}$, which are much higher than the majority phase Ga content. In addition, according to charge balance considerations, the amount of Cs at A sites in the minority phase must be greater than that in the majority. Thus, the Cs concentration at A sites of the minority phase was 20% and 118% higher than the target phase in $Ba_{0.667}Cs_{0.667}Ga_2Ti_6O_{16}$ and $Ba_{1.04}Cs_{0.24}Ga_{2.32}Ti_{5.68}O_{16}$, respectively. In recent work, it was found that high Cs concentrations represent the most thermodynamically favorable state for these hollandite

systems.[18] In light of these findings, one potential explanation of the Ga-rich and Cs-rich phase detected by TXM, could be due to a thermodynamic driving force to form a more stable phase.

The analysis above indicates that the observed rod-like, Ga-rich regions may actually be different stoichiometries/composition of the primary hollandite phase. The heterogeneous nature of this single-phase hollandite could be expected in a solid-state ceramic processing route where a sample's homogeneity is determined by physical mixing coupled with diffusion and (potentially incomplete) phase reaction processes at elevated temperature. This picture of the materials system could explain why only hollandite was detected by lab-based XRD (i.e., because the lattice parameters and changes between the majority and minority phases of the single hollandite phases were too small to detect), while "hot spots" in local Ga composition were detected by TXM and SEM-EDS.

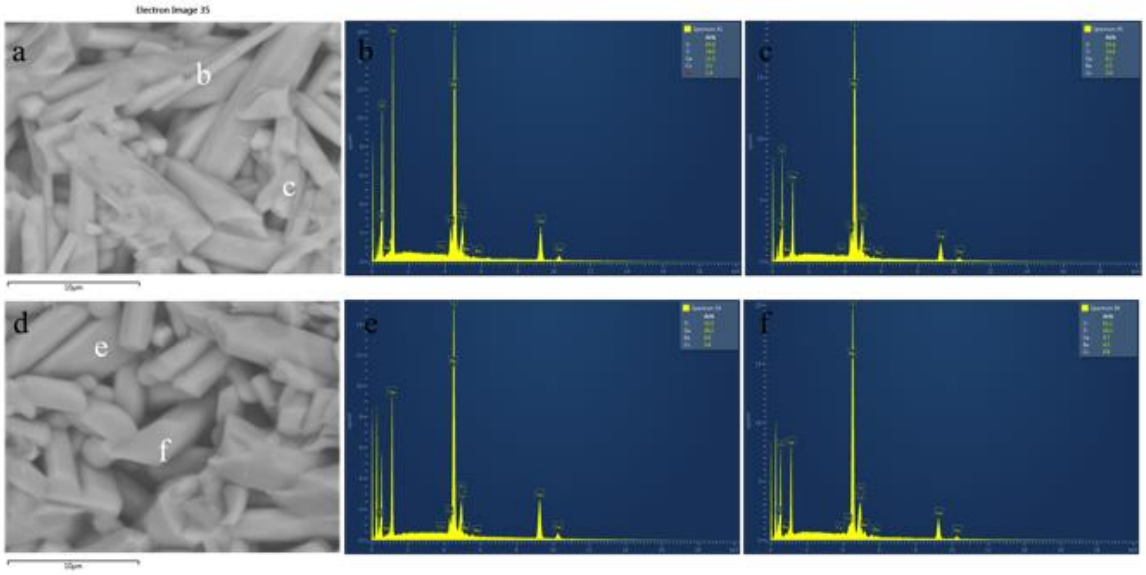

Figure 12: The EDS point result of majority and minority phases are list in a) $Ba_{0.667}Cs_{0.667}Ga_2Ti_6O_{16}$ and b) $Ba_{1.04}Cs_{0.24}Ga_{2.32}Ti_{5.68}O_{16}$.

Table 2: The chemical composition of $Ba_{0.667}Cs_{0.667}Ga_2Ti_6O_{16}$ and $Ba_{1.04}Cs_{0.24}Ga_{2.32}Ti_{5.68}O_{16}$.

	$Ba_{0.667}Cs_{0.667}Ga_2Ti_6O_{16}$			$Ba_{1.04}Cs_{0.24}Ga_{2.32}Ti_{5.68}O_{16}$		
Element	**Target Phase**	**Majority Phase**	**Minority Phase**	**Target Phase**	**Majority Phase**	**Minority Phase**
Ba	0.667	0.633	0.442	1.040	1.010	0.490
Cs	0.667	0.592	0.663	0.240	0.190	0.340
Ga	2.000	1.930	3.630	2.320	2.300	3.980
Ti	6.000	6.000	6.000	5.680	5.680	5.680
O	16.000	16.000	16.000	16.000	16.000	16.000

Using each estimated stoichiometry for the majority and minority hollandite phases, their transmission properties were estimated using the CXRO x-ray calculator and the estimates were compared against the contrast observed in the TXM images. Figure 13 shows the absorption edges calculated for the minority (red), majority (green), and target (blue) hollandite phases. The plots suggest three expectations for the contrast above and below the Ga k-edge: (1) Below the edge, the minority phase absorbs less (and transmits more) than the majority phase and, therefore, should appear darker in the below-edge images (TXM images are presented in "reverse contrast"); (2) Above the edge, the minority phase absorbs more and should appear lighter than the majority phase; and (3) Across the edge, the minority phase's change in contrast should be greater than that of the majority phase (a 7% change in the majority phase versus a 22% change in the minority for the high cesium composition and a 16 versus a 33% change for the lower cesium composition). If the contrast measured in the TXM images is consistent with the three expectations listed above, then the TXM results support the SEM-EDS analysis of the majority and minority hollandite phases.

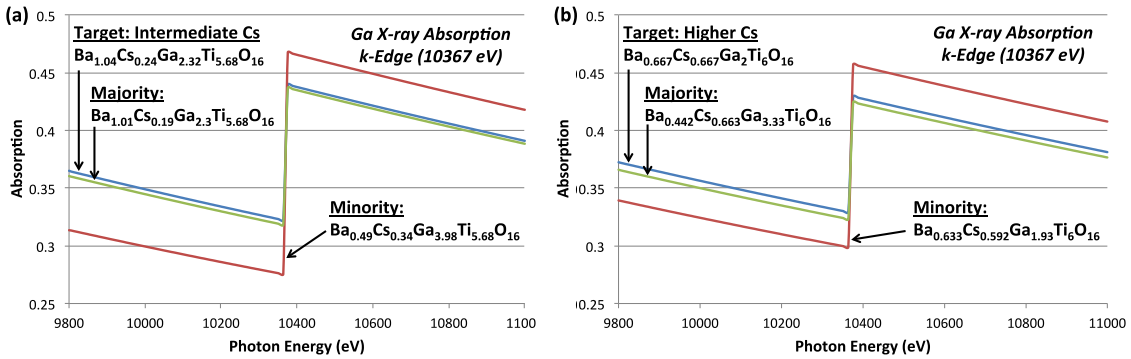

Figure 13: Calculated Ga x-ray absorption k-edges for minority, majority, and target hollandite phases in the intermediate and higher Cs-content single-phase hollandite systems.

The TXM images are in fact consistent with all three of the expectations. For both the literature Cs and high-Cs samples, the minority hollandite phase appears darker in the below-edge image and lighter in the above-edge. Furthermore, the percent changes in contrast for both samples are consistent with those predicted. The minority phase's contrast changed by 27% and 29% in the literature and high-Cs content samples, respectively. The corresponding predicted changes were 33% and 22%. The contrast changes exhibited by the majority phase in the literature and high-Cs content samples were 13% and 12%, respectively, where the corresponding predicted values were 16% and 7%. Exact agreement between the predicted and measured values was not expected because the CXRO calculator does not take into account porosity. Therefore, the TXM results are very much consistent with the SEM-EDS analysis that suggested the presence of a majority and minority composition of the same single-phase hollandite.

Conclusions

In this work, synchrotron-based transmission x-ray microscopy was used to image the 3-D microstructure of multiple phases within model waste form material systems. It was found that Ga doping levels consistent with those commonly used for nuclear waste immobilization ($Ba_{1.04}Cs_{0.24}Ga_{2.32}Ti_{5.68}O_{16}$) could be readily imaged. These results represents an important first step in developing the methods and tools needed to gain an improved understanding of the link between 3-D morphological and chemical features of waste form material microstructures and the corrosion behavior of the materials.

SEM-EDS confirmed the chemical composition of a majority phase and a minority phase in the Ga-doped hollandite waste form material. Three-dimensional absorption contrast TXM images of the samples exhibited contrast changes across the Ga k-edge consistent with the SEM-EDS findings. The analysis suggests that the minority phase is a different stoichiometry/composition of the primary hollandite phase formed by the solid-state ceramic processing route. In future work, complementary techniques, for example (but not limited to) XANES, could be performed to better understand the chemical nature of these phases.

Acknowledgements

The authors are grateful for the support of Nuclear Energy University Program of the US Department of Energy Award ID: DE-NE0008260, CFA-14-6357: "A New Paradigm for Understanding Multiphase Ceramic Waste Form Performance." Portions of this research were carried out at the Stanford Synchrotron Radiation Lightsource, a national user facility operated by Stanford University on behalf of the U.S.

Department of Energy, Office of Basic Energy Sciences. Dr. Ye Lin at the University of South Carolina is gratefully acknowledged for assistance with XPS measurements.

REFERENCES

1 "Waste Forms Technology and Performance Final Report by National Research Council of the National Academies ISBN-10: 0-309-18733-8," *Waste Forms Technol. Perform. Final Rep. by Natl. Res. Counc. Natl. Acad. ISBN-10 0-309-18733-8*, (2011).

2 A. Ringwood, S. Kesson, N. Ware, W. Hibberson, and A. Major, "Immobilization of High-Level Nuclear-Reactor Wastes in SYNROC," *Nature*, **278** 219–223 (1979).

3 A.E. Ringwood, S.E. Kesson, N.G. Ware, W.O. Hibberson, and A. Major, "SYNROC PROCESS - GEOCHEMICAL APPROACH TO NUCLEAR WASTE IMMOBILIZATION," *Geochem. J.*, **13** [4] 141–165 (1979).

4 C. Natl Res, *Waste Forms Technology and Performance: Final Report*. Natl Academies Press, Washington, 2011.

5 R.A. Kerr, "NUCLEAR WASTE-DISPOSAL - ALTERNATIVES TO SOLIDIFICATION IN GLASS PROPOSED," *Science (80-.).*, **204** [4390] 289–291 (1979).

6 K. Brinkman, K. Fox, J. Marra, and M. Tang, "Crystalline Ceramic Waste Forms: Reference Formulation Report," *Savannah River Natl. Lab. Tech. Rep. SRNL-STI-2012-00281, FCRD-SWF-2012-000116*, (2012).

7 M.L. Carter, A.L. Gillen, K. Olufson, and E.R. Vance, "HIPed Tailored Hollandite Waste Forms for the Immobilization of Radioactive Cs and Sr," *J. Am. Ceram. Soc.*, **92** [5] 1112–1117 (2009).

8 A. Cleave, R.W. Grimes, and K. Sickafus, "Plutonium and uranium accommodation in pyrochlore oxides," *Philos. Mag.*, **85** [9] 967–980 (2005).

9 K. Brinkman, J. Amoroso, J. Marra, and M. Tang, "Crystalline Ceramic Waste Forms: Comparison of Reference Process for Ceramic Waste Form Fabrication," *SRNL Tech. Report- FCRD-SWF-2013-000229*, (2013).

10 E.R. Vance, G.R. Lumpkin, M.L. Carter, D.J. Cassidy, C.J. Ball, R.A. Day, and B.D. Begg, "Incorporation of uranium in zirconolite (CaZrTi2O7)," *J. Am. Ceram. Soc.*, **85** [7] 1853–1859 (2002).

11 S. V Stefanovsky, A.G. Ptashkin, O.A. Knyazev, S.A. Dmitriev, S. V Yudintsev, and B.S. Nikonov, "Inductive cold crucible melting of actinide-bearing murataite-based ceramics," *J. Alloys Compd.*, **444** 438–442 (2007).

12 A. V Demine, N. V Krylova, P.P. Polyektov, I.N. Shestoperov, T. V Smelova, V.F. Gorn, and G.M. Medvedev, "High level liquid waste solidification using a 'cold' crucible induction melter"; pp. 27–33 in *Sci. Basis Nucl. Waste Manag. Xxiv*. Edited by K.P. Hart and G.R. Lumpkin. Materials Research Society, Warrendale, 2000.

13 T. Advocat, G. Leturcq, J. Lacombe, G. Berger, R.A. Day, K. Hart, E. Vernaz, and

A. Bonnetier, “Alteration of cold crucible melter titanate-based ceramics: Comparison with hot-pressed titanate-based ceramic;” pp. 355–362 in *Sci. Basis Nucl. Waste Manag. Xx*. Edited by W.J. Gray and I.R. Triay. Materials Research Society, Warrendale, 1997.

14 A.P. Cocco, G.J. Nelson, W.M. Harris, A. Nakajo, T.D. Myles, A.M. Kiss, J.J. Lombardo, and W.K.S. Chiu, “Three-dimensional microstructural imaging methods for energy materials.,” *Phys. Chem. Chem. Phys.*, **15** [39] 16377–16407 (2013).

15 J.S. Cronin, Y.K. Chen-Wiegart, J. Wang, and S.A. Barnett, “Three-dimensional reconstruction and analysis of an entire solid oxide fuel cell by full-field transmission X-ray microscopy,” *J. Power Sources*, **233** 174–179 (2013).

16 M.L. Carter, E.R. Vance, D.R.G. Mitchell, J. V Hanna, Z. Zhang, and E. Loi, “Fabrication, characterization, and leach testing of hollandite, (Ba,Cs)(Al,Ti)(2)Ti6O16,” *J. Mater. Res.*, **17** [10] 2578–2589 (2002).

17 J. Amoroso, J. Marra, S.D. Conradson, M. Tang, and K. Brinkman, “Melt processed single phase hollandite waste forms for nuclear waste immobilization: Ba(1.0)Cs(0.3)A(2.3)Ti(5.7)O(16); A = Cr, Fe, Al,” *J. Alloys Compd.*, **584** 590–599 (2014).

18 Y. Xu, Y. Wen, R. Grote, J. Amoroso, L.S. Nickles, and K.S. Brinkman, “A-site compositional effects in Ga-doped hollandite materials of the form BaxCsyGa2x+ yTi8− 2x− yO16: implications for Cs immobilization in crystalline ceramic waste forms,” *Sci. Rep.*, **6** 27412 (2016).

19 A.C. Kak and M. Slaney, *Principles of Computerized Tomographic Imaging*. Society of Industrial and Applied Mathematics, 2001.

20 A. Markoe, *Analytic Tomography*. Cambridge Univ Press, 2006.

21 J.R. Izzo, Jr., A.S. Joshi, K.N. Grew, W.K.S. Chiu, A. Tkachuk, S.H. Wang, and W. Yun, “Nondestructive Reconstruction and Analysis of SOFC Anodes Using X-ray Computed Tomography at Sub-50 nm Resolution,” *J. Electrochem. Soc.*, **155** [5] B504–B508 (2008).

22 K.N. Grew, Y.S. Chu, J. Yi, A.A. Peracchio, J.R. Izzo, Jr., Y. Hwu, F. De Carlo, and W.K.S. Chiu, “Nondestructive Nanoscale 3D Elemental Mapping and Analysis of a Solid Oxide Fuel Cell Anode,” *J. Electrochem. Soc.*, **157** [6] B783–B792 (2010).

23 J.J. Lombardo, R.A. Ristau, W.M. Harris, and W.K.S. Chiu, “Focused ion beam preparation of samples for X-ray nanotomography.,” *J. Synchrotron Radiat.*, **19** [Pt 5] 789–796 (2012).

24 Y. Xu, M. Feygenson, K. Page, L. Shuller-Nickles, and K. Brinkman, “Structural Evolution in Hollandite Solid Solutions Across the A-site Compositional Range from Ba1.33Ga2.66Ti5.34O16 to Cs1.33Ga1.33Ti6.67O16,” *J. Am. Ceram. Soc.*, **Accepted** (2016).

25 T. Suzuki-Muresan, J. Vandenborre, A. Abdelouas, B. Grambow, and S. Utsunomiya, “Studies of (Cs, Ba)-hollandite dissolution under gamma irradiation at 95° C and at pH 2.5, 4.4 and 8.6,” *J. Nucl. Mater.*, **419** [1] 281–290 (2011).

26 S.E. Kesson and T.J. White, “Radius Ratio Tolerance Factors and the Stability of Hollandite,” *J. Solid State Chem.*, **63** [1] 122–125 (1986).

27 C. Gionco, S. Livraghi, S. Maurelli, E. Giamello, S. Tosoni, C. Di Valentin, and G.

Pacchioni, “Al- and Ga-Doped TiO2, ZrO2, and HfO2: The Nature of O 2p Trapped Holes from a Combined Electron Paramagnetic Resonance (EPR) and Density Functional Theory (DFT) Study,” *Chem. Mater.*, **27** [11] 3936–3945 (2015).

Supplemental:

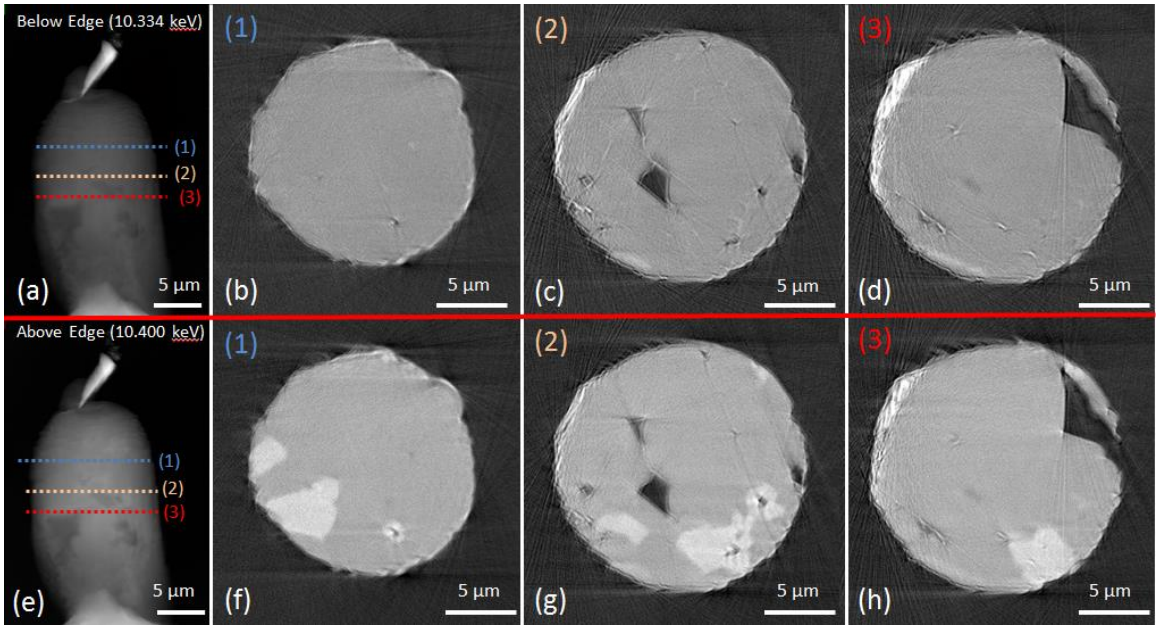

Figure S1: Baseline single-phase hollandite without Cs ($Ba_{1.33}Ga_{2.66}Ti_{5.34}O_{16}$). Sample was milled using a plasma FIB with Xe ion beam (FEI Helios PFIB).

Figure S1 shows a baseline single-phase hollandite waste form sample ($Ba_{1.33}Ga_{2.66}Ti_{5.34}O_{16}$) that was prepared using a Xe plasma FIB rather than the Ga FIB used to prepare the previous samples. The images obtained from this sample are virtually identical to those obtained from the sample milled using a Ga FIB, which rules out the possibility that the Ga-rich regions observed in the material are the result of Ga implantation during the FIB milling process.